Science Advances
AAAS

Supplementary Materials for

Toughening mechanisms for the attachment of architectured materials: The mechanics of the tendon enthesis

Mikhail Golman, Adam C. Abraham, Iden Kurtaliaj, Brittany P. Marshall,
Yizhong Jenny Hu, Andrea G. Schwartz, X. Edward Guo, Victor Birman,
Philipp J. Thurner, Guy M. Genin*, Stavros Thomopoulos*

*Corresponding author. Email: sat2@columbia.edu (S.T.); genin@wustl.edu (G.M.G.)

Published 26 November 2021, *Sci. Adv.* **7**, eabi5584 (2021)
DOI: 10.1126/sciadv.abi5584

The PDF file includes:

Figs. S1 to S20
Supplementary Text
Table S1
Legends for movies S1 to S4
References

Other Supplementary Material for this manuscript includes the following:

Movies S1 to S4

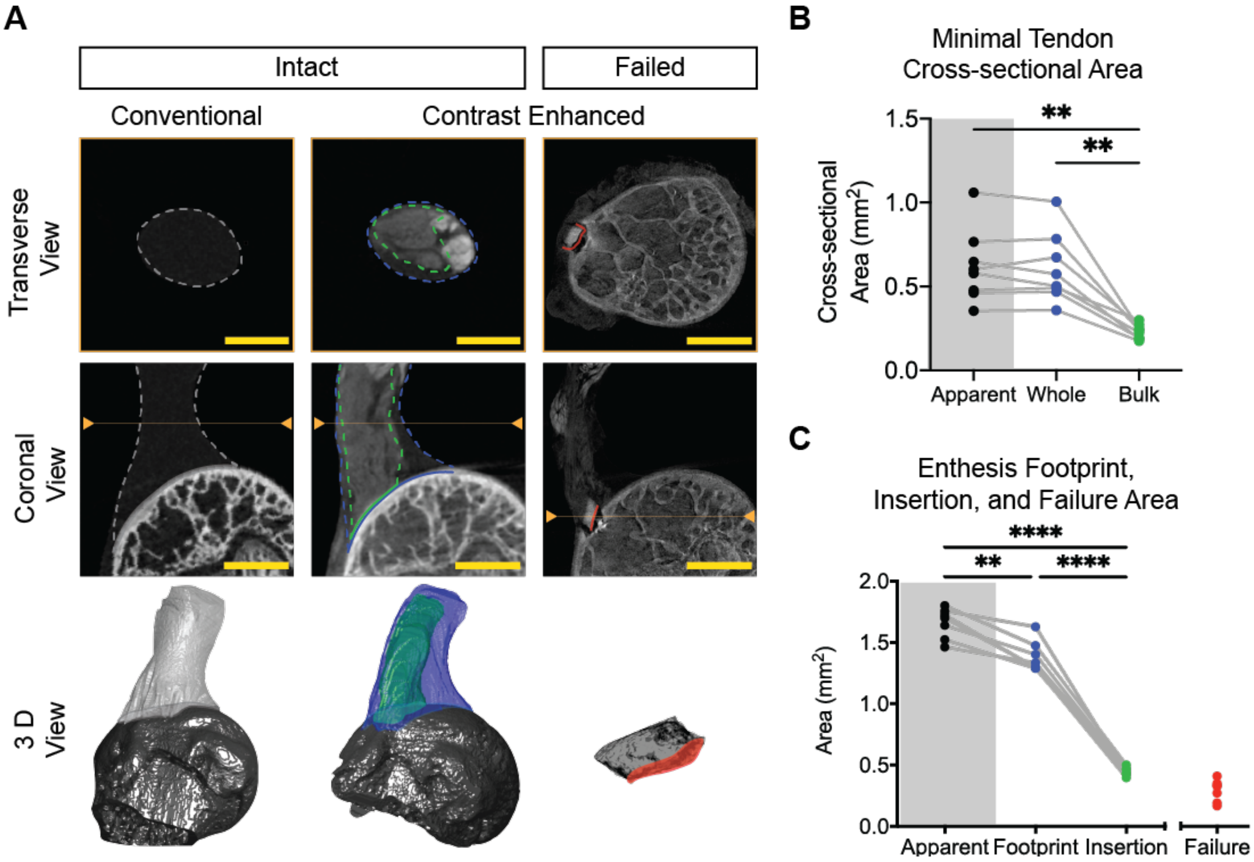

Fig. S1. Tendon cross-sectional area, tendon enthesis footprint area, primary insertion, and failure area.

(A) Intact and post-failure images of the tendon enthesis were obtained by conventional and contrast enhanced high resolution micro computed tomography (microCT). The location of the images shown in the transverse view are indicated by the line within the orange arrow heads in the coronal view images. The 3D view was generated using MATLAB from volume contouring and rendering. 2D image scale bars are 800 μm for all images. 3D representations are not to scale. (B) Minimal tendon cross-sectional area was obtained from microCT images. "Apparent" area, shown in the gray shaded region, was obtained using conventional microCT; all other measurements were obtained using contrast enhanced microCT. (** $p<0.01$, repeated measures ANOVA followed by the Tukey's multiple comparison test). (C) The enthesis footprint, insertion, and failure areas were obtained from microCT images of the tendon enthesis. "Apparent" area, shown in the gray shaded region, was obtained using conventional microCT; all other measurements were obtained using contrast enhanced microCT. (*** $p<0.001$, repeated measures ANOVA followed by the Tukey's multiple comparison test).

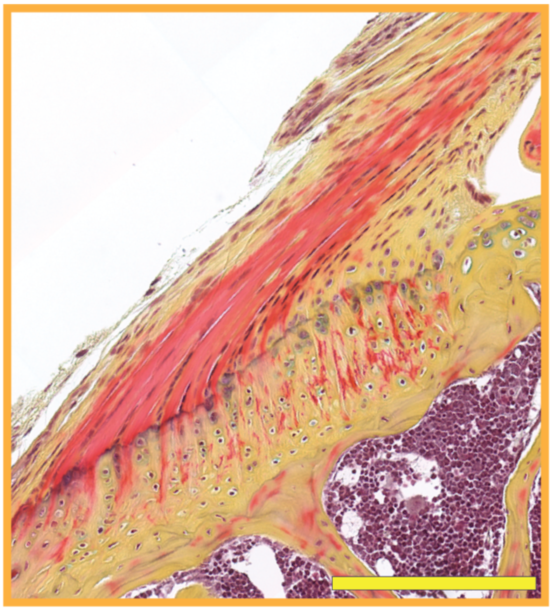

Fig. S2. Representative image of pentachrome-stained coronal section of the tendon enthesis.

Red stain shows mature collagen fibers, yellow stain shows mineralized tissue and connective tissue. Scale bar represents scale bars are 200 µm. The newly found primary insertion directly corresponded to the region stained in red.

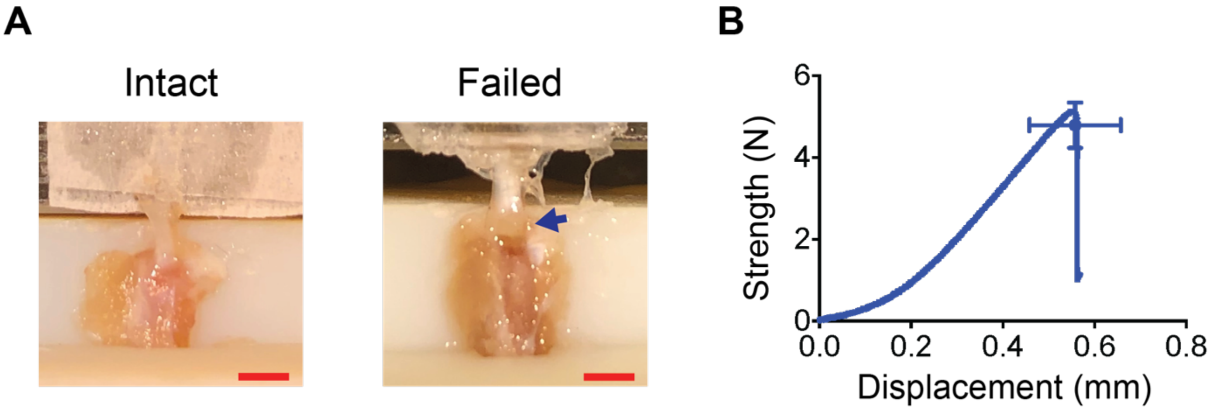

Fig. S3. Tendon enthesis samples failed catastrophically.

(A) A representative murine tendon enthesis sample is shown before and after mechanical testing (scale bars: 2 mm). While the majority of the primary insertion was avulsed, peritenon tissue surrounding the primary insertion site was still attached post failure (blue arrow). (B) A representative tendon enthesis strength (force) vs. displacement curve is shown for a uniaxial quasi-static test to failure. The mean failure strength (force) and failure displacement are represented by the blue dot (cross-head represents standard deviations).

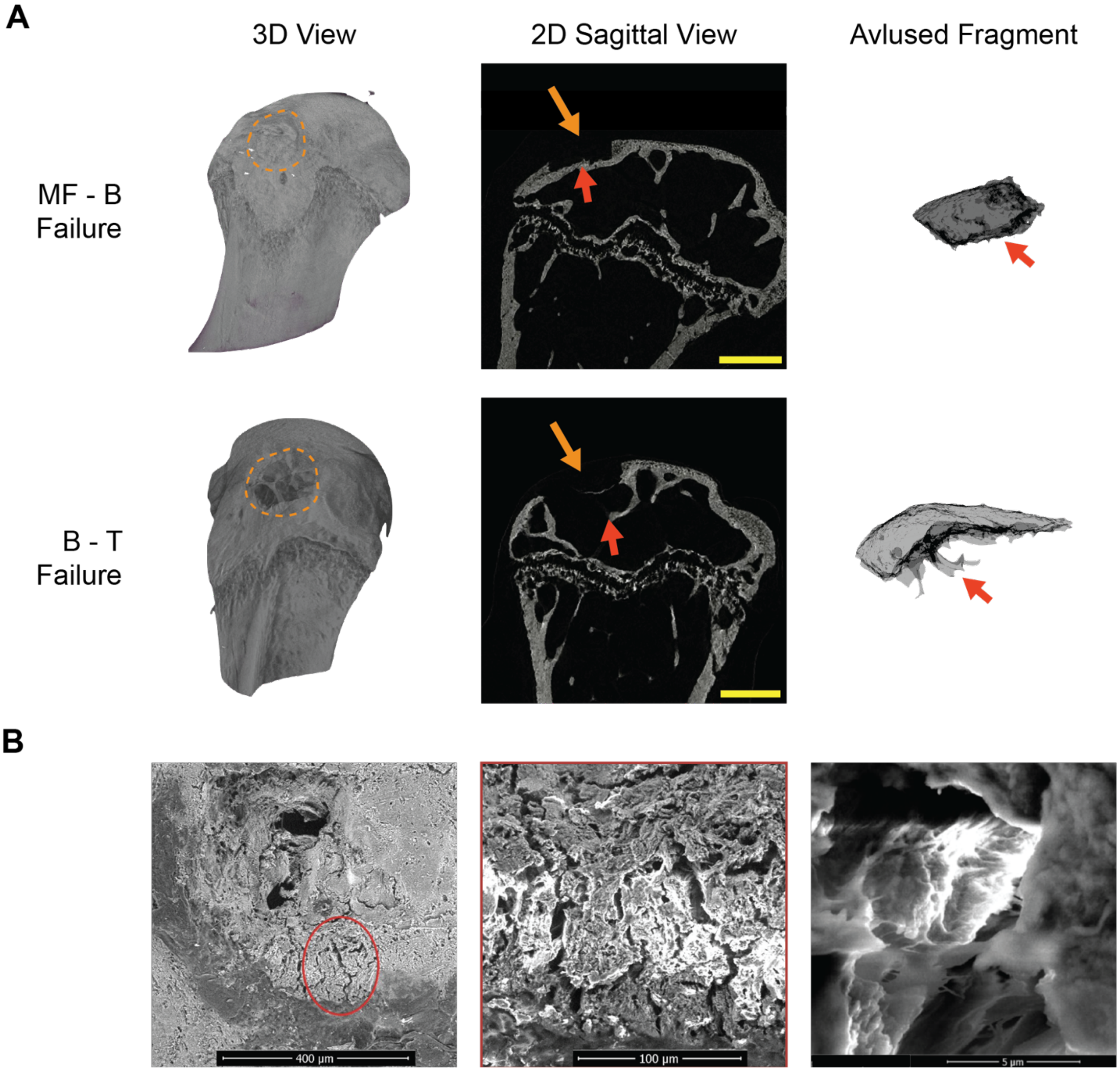

Fig. S4. Tendon enthesis failed with a failure crater at the attachment site.

(A) Conventional microCT imaging of post-failure humeral head samples (3D rendering and 2D sagittal view) and 3D visualization of avulsed fragment are shown. Tendon entheses failed either at the interface between mineralized fibrocartilage and bone (MF-B failure type), or in the underlying trabecular bone (B-T failure type) (scale bars: 500 µm). The orange dashed outline and the orange arrows indicate the site of the entheses attachments pre-failure and the humeral head cater post-failure. Red arrows indicate fracture (failure) surfaces. (B) Scanning electron microscopy images of failed tendon enthesis samples are shown, focused on the humeral head crater. Crack propagation around the avulsion site was noted. Images were obtained in BSE mode.

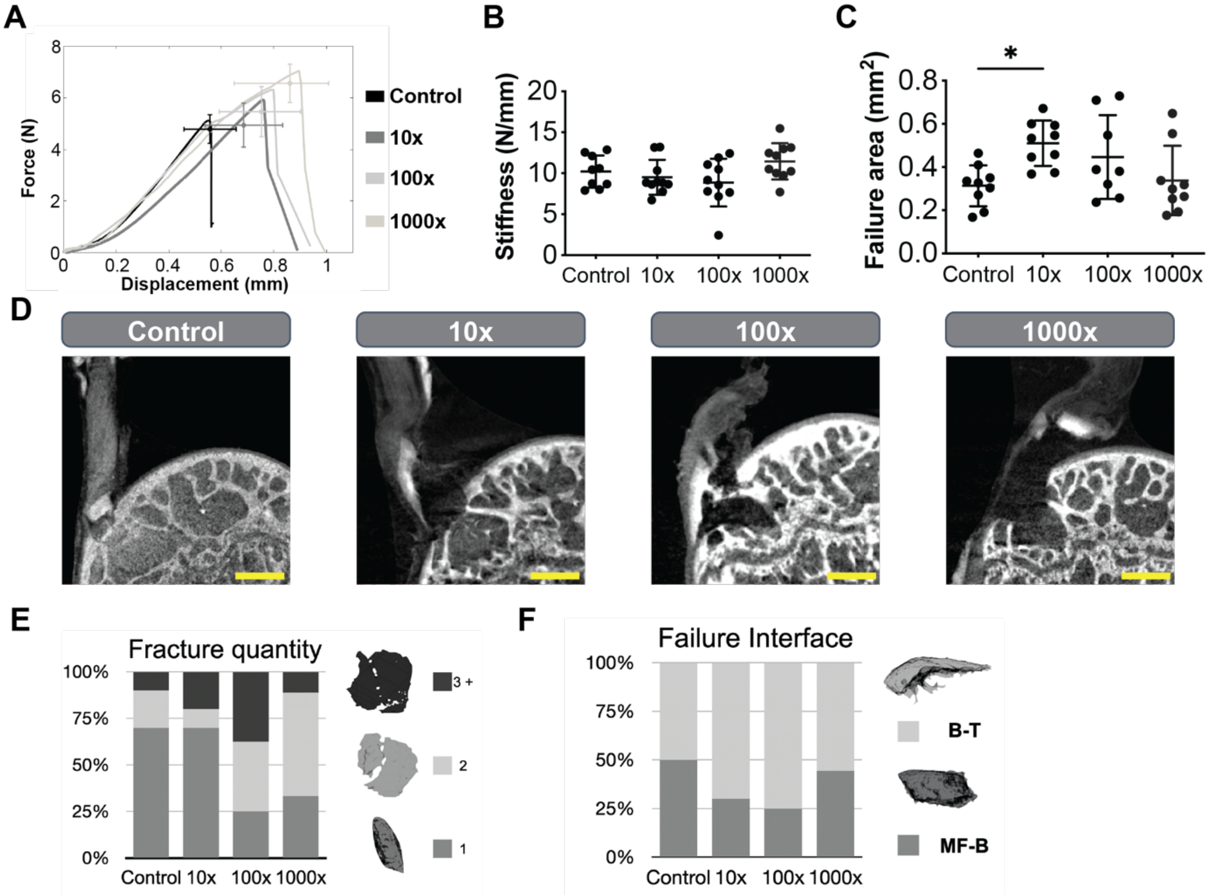

Fig. S5. Mechanical and failure responses of the tendon entheses in response to acute loading (monotonic tension across a range of loading rates).

(A) Representative force-displacement curves for monotonic loadings are shown. (B) Stiffness was not affected by increase in strain rates. (C), Avulsed (failed/fractured) area increased with loading rate. (* $p<0.05$, ANOVA followed by the Tukey's multiple comparison test). (D) Representative contrast enhanced images of failed samples are shown for all loading rates (scale bars: 250 μm). (E) Avulsed (fractured) quantity distribution increased with increasing loading rate. (F) Failure interface (MF-B vs. B-T) did not significantly change with increasing loading rate.

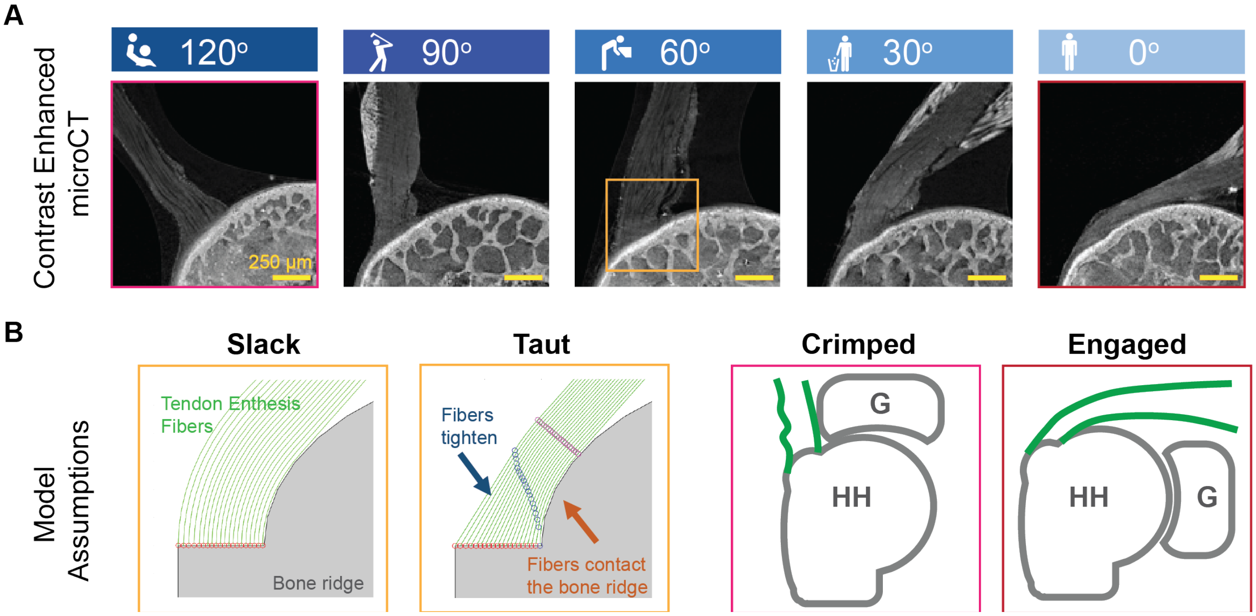

Fig. S6. Imaging based positional-recruitment model assumptions.

(A) High-resolution contrast-enhanced images of samples are shown at each abduction angle tested (scale bars: 250 µm). (B) The positional recruitment model assumed that: (1) fiber length increases with the distance from the bone ridge and (2) fibers get taught once they are engaged (red points to blue points). Depending on loading direction, fibers come into contact with their neighboring fibers or the humeral head and affected by their curvature (blue points to purple points). This allowed for the representation of all fibers as taut at low angles of abduction (0°-30°) and some fibers intrinsically initially buckled at high angles of abduction (90°-120°). Green: tendon fibers, gray: humeral head bone ridge. G: glenoid, HH: humeral head.

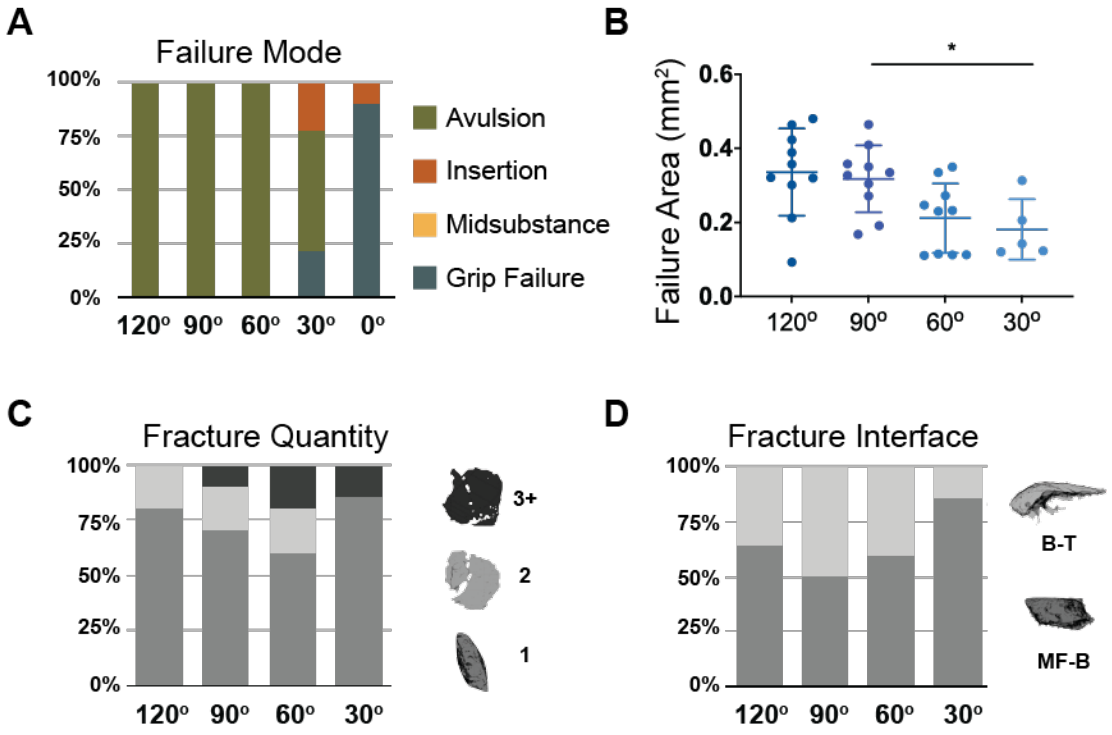

Fig. S7. Tendon enthesis failure behavior depended strongly on the angle of abduction.

(A) Samples failed primarily via bony avulsion. However, at low angle of abductions (0°-30°), most samples failed at the grips. (B) The size of the fractured area decreased at low angles of abduction ($p<0.01$). (C) There was a shift towards MF-B type failure when samples were pulled at 30° of abduction. (D) Fragment quantity distribution did not show a trend with loading angle.

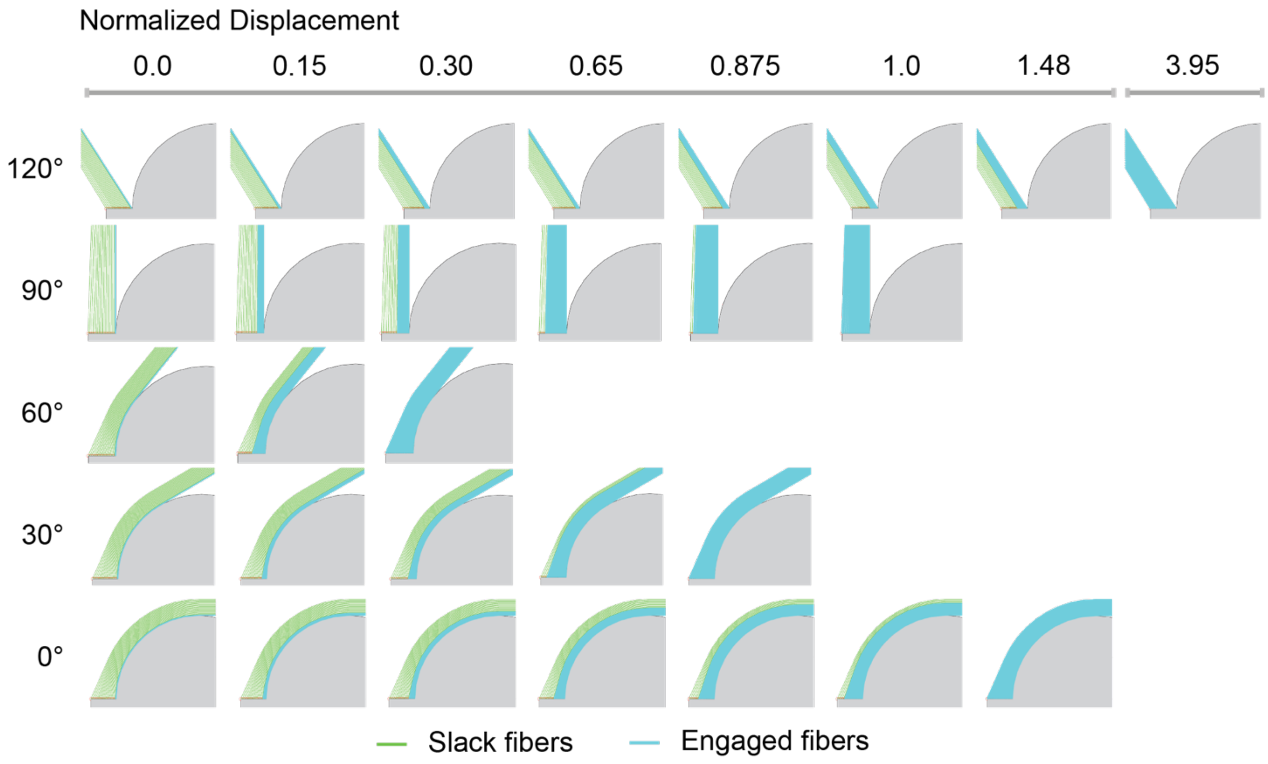

Fig. S8. Spatial distribution of fiber engagement for each abduction angle at representative normalized displacements.

Snapshots of positional-recruitment model outputs are plotted at representative normalized displacements for each abduction angle. The displacement was normalized against the displacement when tendon enthesis full recruitment was achieved at 90°. Simulations revealed that innermost fibers engage first at every abduction angle simulated. Green shows slack fibers and blue shows engaged fibers at each representative normalized displacements.

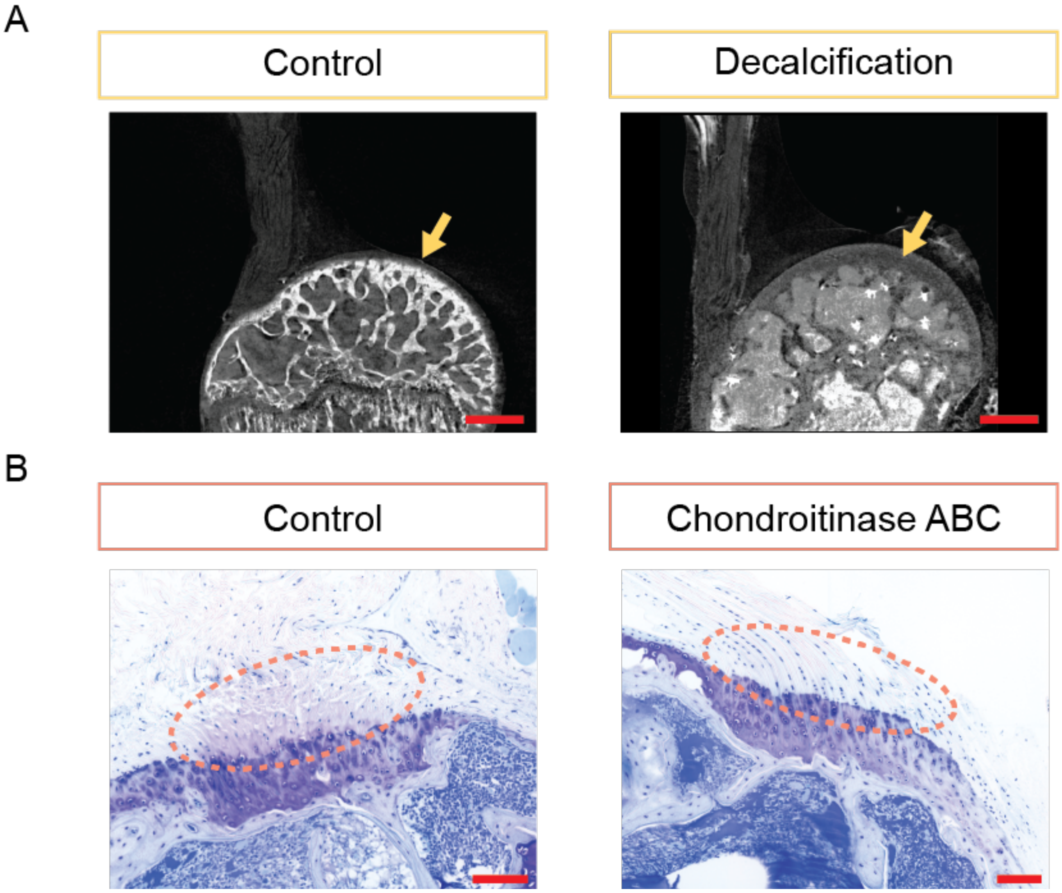

Fig. S9. Both protocols were effective in removing constituents of the tendon enthesis.

(A) Contrast enhanced microCT imaging showed that formic acid treatment completely removed the mineral from the tendon enthesis and the humeral head bone (scale bars: 500 µm). Yellow arrows indicate changes in the coefficient of attenuation due to the mineral loss in the sample. (B) Alcian blue staining of the tendon enthesis showed that chondroitinase ABC treatment removed proteoglycan components from the unmineralized portion of the enthesis (change in staining outlined by orange dashed ellipsoid; scale bar: 100 µm).

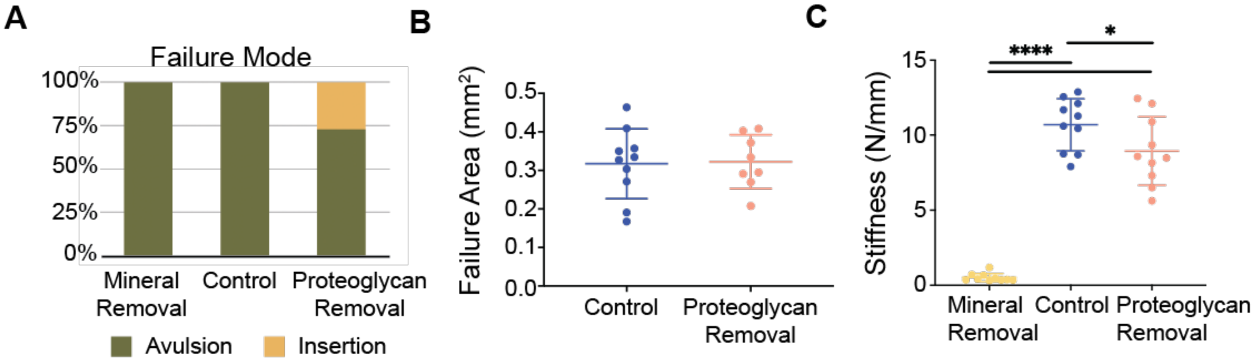

Fig. S10. Loss of mineral or proteoglycan did not significantly alter the failure modes of the tendon enthesis, while changes in the tendon enthesis stiffness were observed.

(A) Removal of mineral or proteoglycan did not significantly alter the tendon enthesis failure mode. (B) There were no significant differences in failure (avulsed) area due to removal of proteoglycans. Note that the failure (avulsed) area for demineralized enthesis samples was not obtainable with current methodologies. (C), Removal of mineral or proteoglycan led to significant differences changes in stiffness. (* $p<0.05$, **** $p<0.0001$, ANOVA followed by the Dunnett's multiple comparison test).

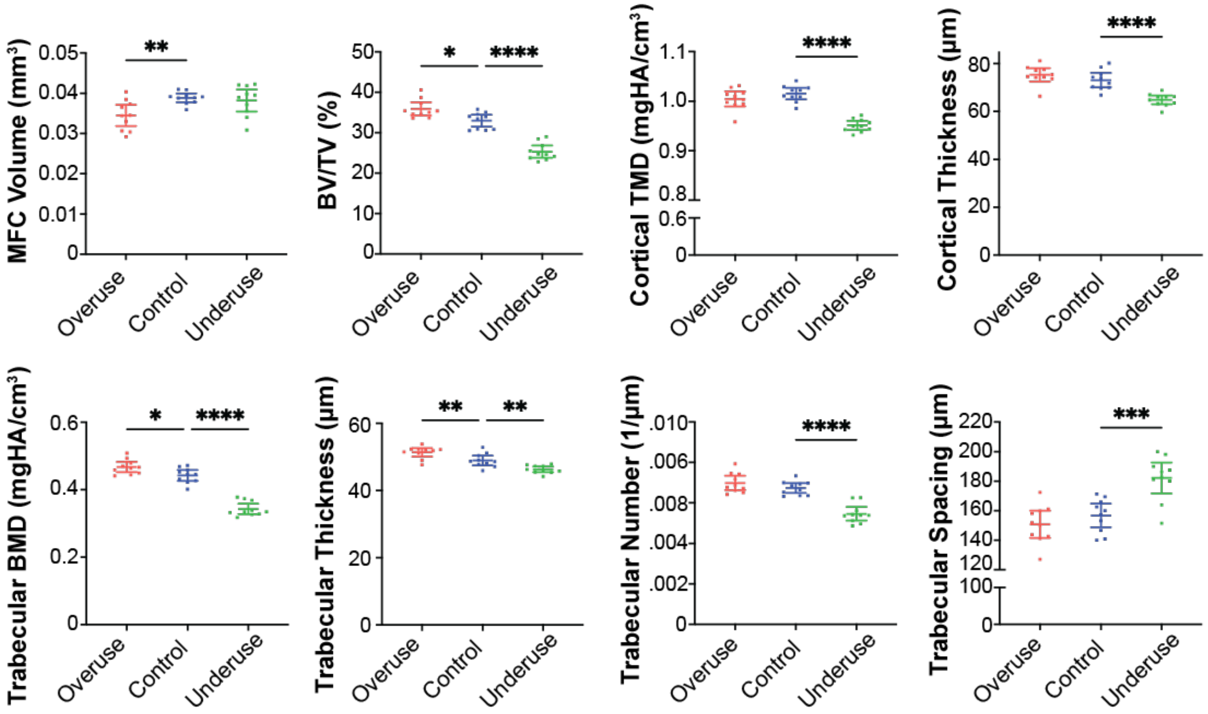

Fig. S11. Pathologic loading led to adaptations in mineralized fibrocartilage and bone architecture underlying the tendon enthesis.

MicroCT analysis revealed that overuse degeneration led to decrease in mineralized fibrocartilage volume (MFC volume, $p<0.01$). Bone morphometric analysis revealed that underuse led to loss of bone mineral density underlying the attachment (BMD and TMD, $p<0.0001$), reduced cortical and trabecular thickness($p<0.0001$), and trabecular number ($p<0.001$). Overuse degeneration led to gain of bone volume in the humeral head (BV/TV, $p<0.05$), trabecular mineral density (BMD, $p<0.05$), and increase in trabecular thick-ness ($p<0.01$). (* $p<0.05$, ** $p<0.01$, *** $p<0.001$, **** $p<0.0001$, ANOVA followed by the Dunnett's multiple comparison test).

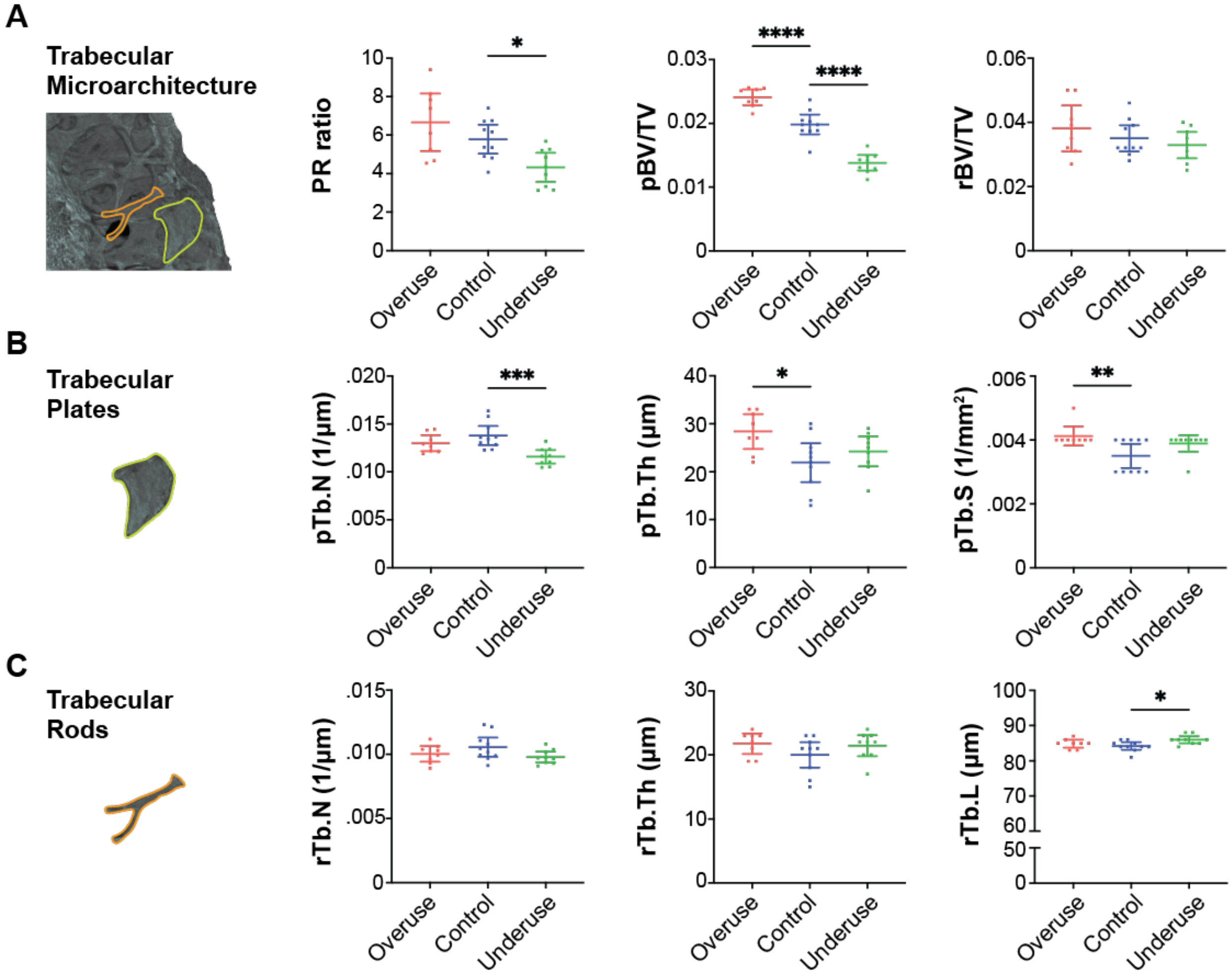

Fig. S12. Local changes in trabecular microarchitecture underlying the tendon enthesis.

(A) Individual trabecula segmentation (ITS) analysis showed that the ratio between trabecular plates and trabecular rods significantly decreased due to underuse compared to control ($p<0.05$). Trabecular plate volume significantly decreased due to underuse ($p<0.0001$) and significantly increased due to overuse ($p<0.0001$) compared to control. There were no significant differences between groups in trabecular rod volume. **(B)** Trabecular plate analysis showed that the number of trabecular plates (pTb.N) significantly decreased due to underuse ($p<0.0001$), while trabecular plate thickness (pTb.Th) and surface area (pTb.S) significantly increased due to overuse ($p<0.05$). **(C)** Trabecular rod analysis showed that there were no differences in rod number (rTb.N) thickness (rTb.Th). However, the length of trabecular rods (rTb.L) significantly increased due to underuse compared to that of control ($p<0.05$). (* $p<0.05$, ** $p<0.01$, *** $p<0.001$, **** $p<0.0001$, ANOVA followed by the Dunnett’s multiple comparison test).

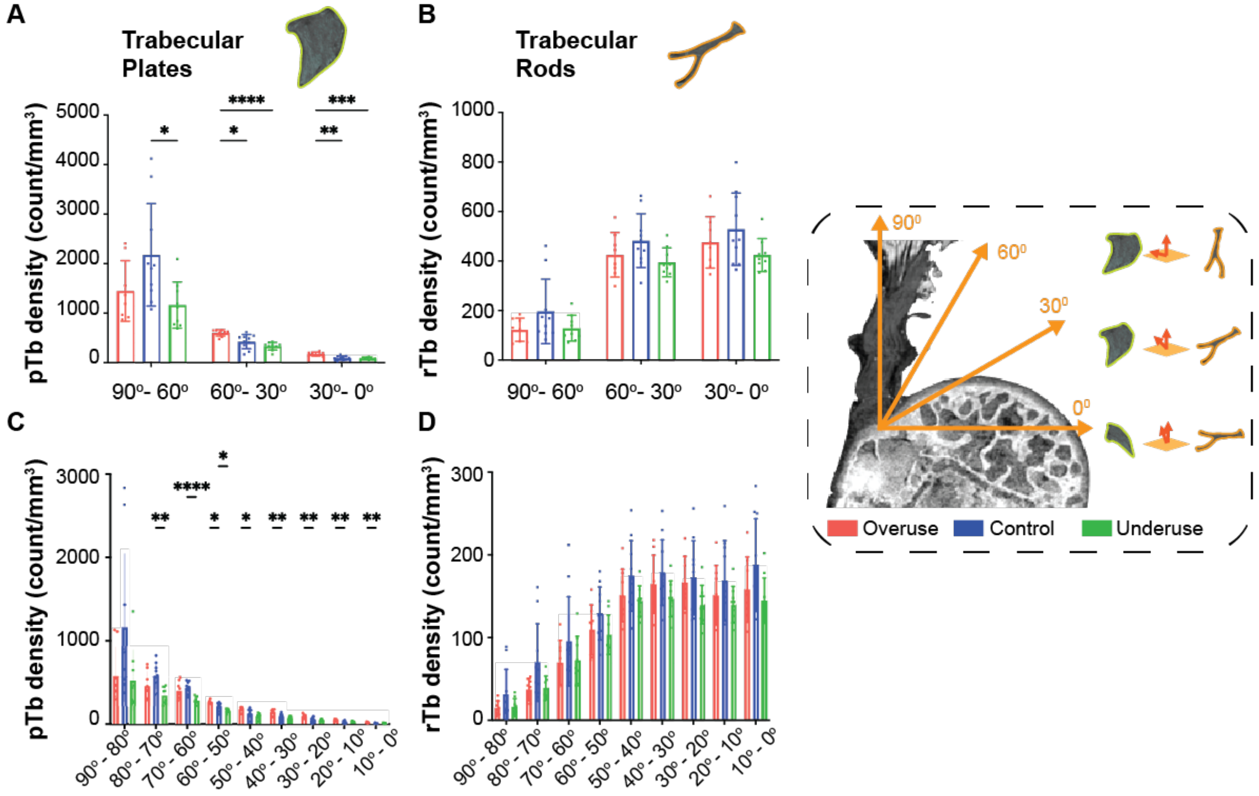

Fig. S13. The orientation analysis of trabecular microarchitecture underlying the tendon enthesis.

(A)-(B), Coarse orientation analysis is shown for (A) trabecular plates and (B) trabecular rods. **(C)-(D),** Fine orientation analysis is shown for (C) trabecular plates and (D) trabecular rods. The angle was taken with the axis normal to the supraspinatus tendon insertion surface. (* $p<0.05$, ** $p<0.01$, **** $p<0.0001$, 2-way ANOVA followed by Dunnet's multiple comparison test).

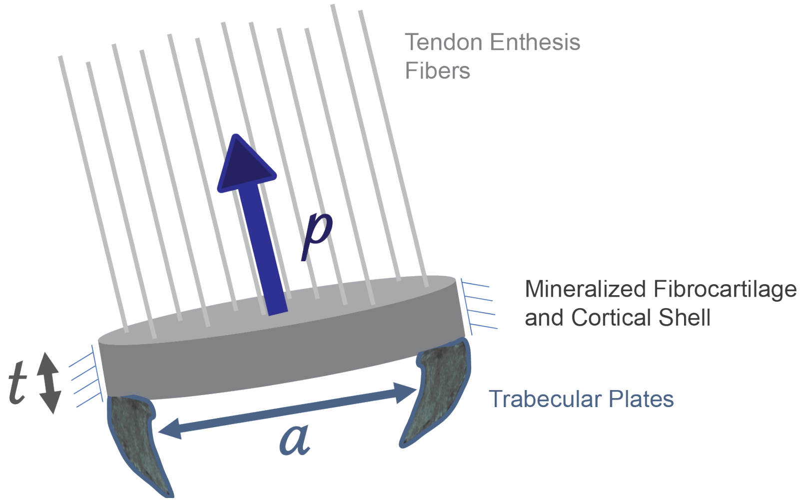

Fig. S14. Enthesis fracture model.

A first order model of tendon enthesis failure behavior was developed. The tendon enthesis was modeled as a circular, clamped plate loaded with uniform pressure. In this model, $\boldsymbol{a}$ is distance between clamps (i.e., trabecular spacing), $\boldsymbol{p}$ is the applied pressure (i.e., force), and $\boldsymbol{t}$ is the plate thickness (i.e., mineralized thickness).

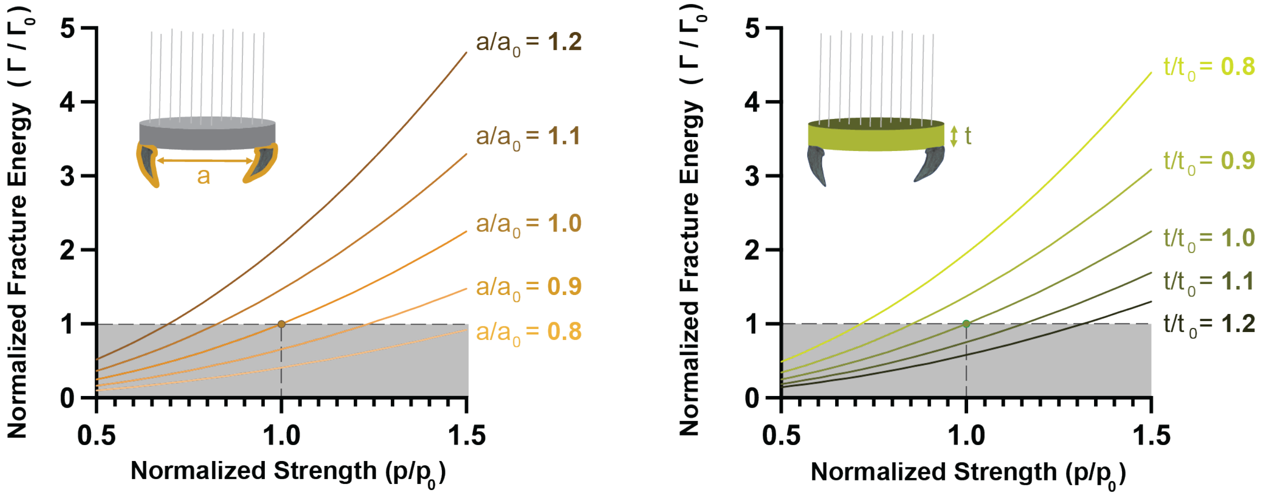

Fig. S15. Bony microarchitecture underlying the enthesis is optimized for tendon enthesis toughness: a small increase in strength leads to significant gain in energy absorption at the time of enthesis fracture.

The relationship between normalized fracture energy (Γ/Γ_0) and trabecular spacing, Tb.Sp, (a/a_0) or mineralized bony base thickness (t/t_0) was plotted against normalized strength (p/p_0).

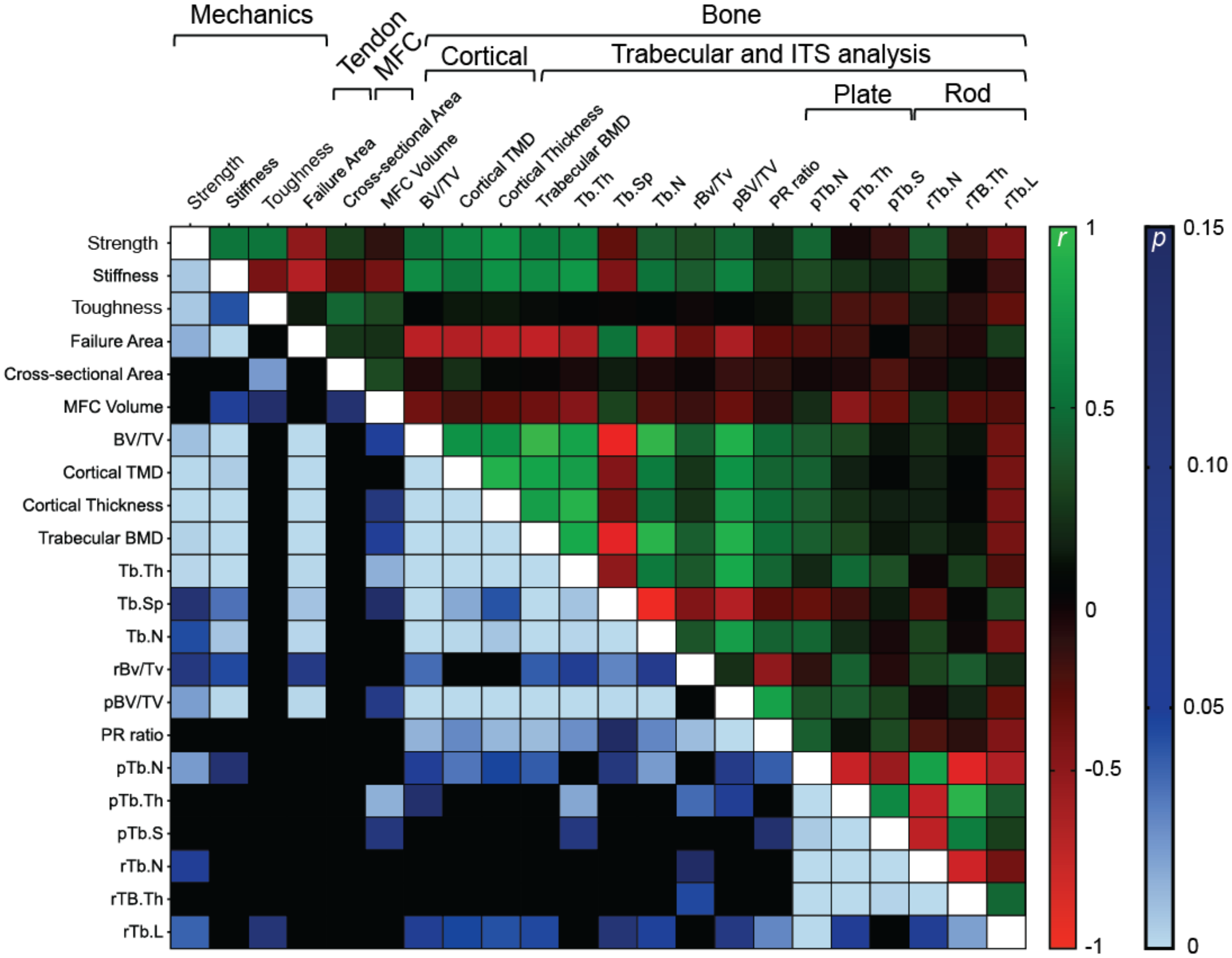

Fig. S16. Pearson correlation results obtained from enthesis mechanical behavior, enthesis failure behavior, enthesis characteristics, and bony architecture under the enthesis.

Green represents a positive correlation, while red represents an inverse correlation. Blue gradient show p values.

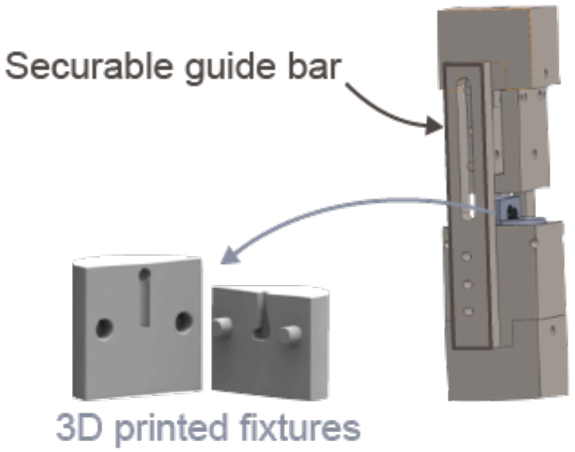

Fig. S17. Gripping mechanism used for the mechanical testing of tendon entheses.
3D printed fixtures and gripping mechanism used for the mechanical testing protocols.

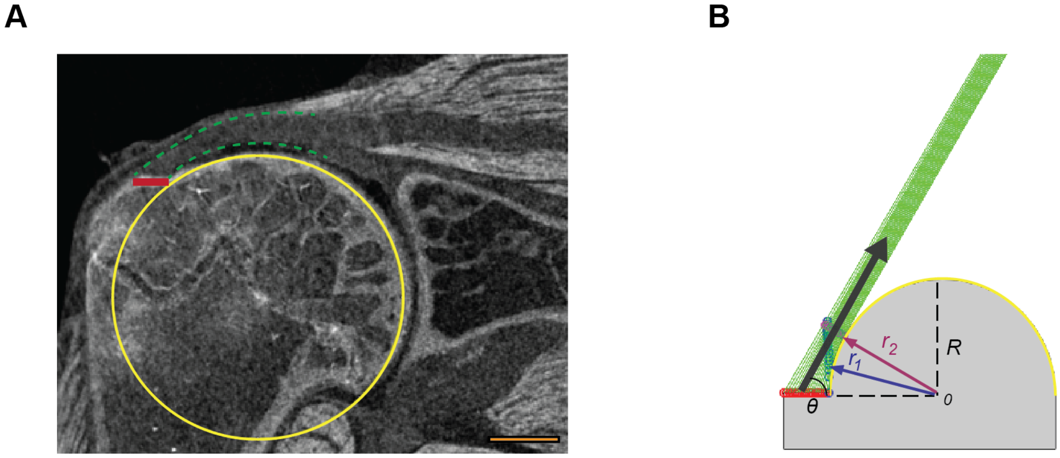

Fig. S18. Positional-recruitment model.

(A) Representative contrast enhanced image of the tendon enthesis is shown (scale bar: 500 µm). The orange line indicates the attachment footprint and the yellow circle outlines the circular anatomy of the humeral head. **(B)** A schematic of the positional-recruitment model is shown. Green lines represent enthesis fibers, the gray surface represents the humeral head bone, and the black arrow indicates the direction of the pull. At rest, the outer fibers are longer than the inner fibers. If a fiber is engaged and oriented so that it contacts the bone, it tightens until it reaches the tangent point to the humeral head curvature (blue circles) and the tangent point to the tendon fiber (magenta circles). Dark gray arrow represents loading direction.

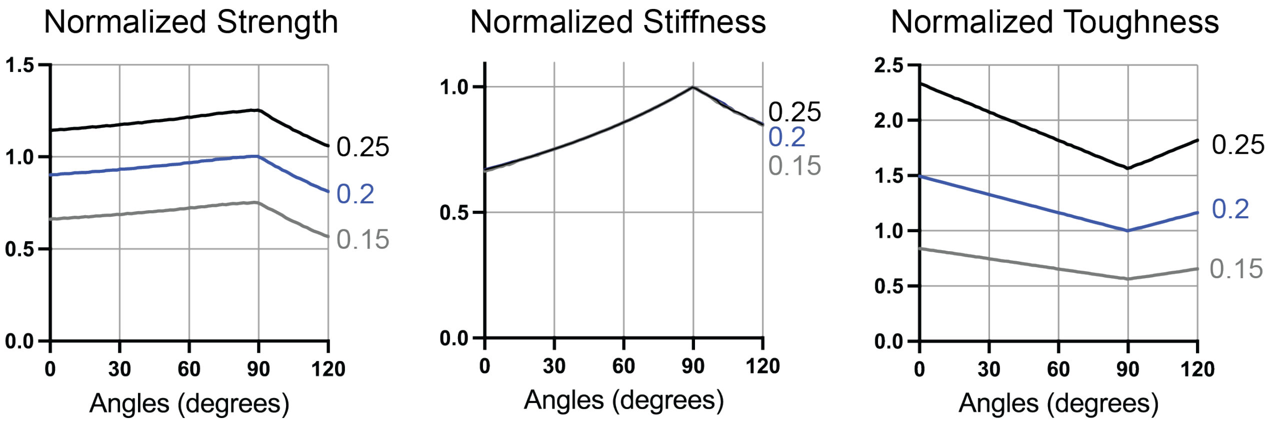

Fig. S19. Dependence of positional-recruitment model outputs on fiber failure strain. Normalized strength, stiffness, and toughness were plotted for a range of loading directions. Simulations were run with model parameters presented in Table S1, except fiber failure strain was varied (0.15, 0.2, and 0.25). Output results were normalized against the condition where tightly packed fibers (s/t=1) with initial length matched to the shortest tendon enthesis fiber (the innermost fiber), and fiber failure strain of 0.2, were stretched uniaxially at 90° of abduction.

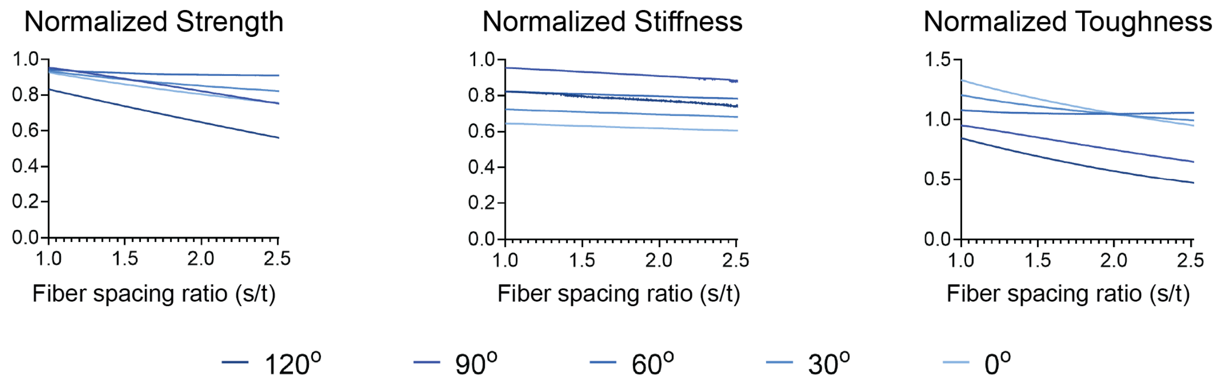

Fig. S20. Dependence of positional-recruitment model outputs on fiber spacing.

Normalized strength, stiffness, and toughness were plotted against the distance between fibers (s/t). Simulations were run with model parameters presented in Table S1, except distance between fibers, *s*, was varied. Output results were normalized against the condition where tightly packed fibers (s/t=1) with initial length matched to the shortest tendon enthesis fiber (the innermost fiber) were stretched uniaxially at 90° of abduction.

Supplementary Text

Notes on contrast enhanced microCT scanning and enthesis visualization

While contrast enhancement was non-reversible, the technique was non-destructive; when testing for shrinkage or damage due to processing, the values obtained for whole tendon cross-sectional area for contrast-enhanced samples matched the measurements obtained prior to submerging in mercury (II) chloride solution (apparent cross-sectional area) (Fig. S1). At the site of minimal tendon cross-sectional area, approximately 500 μm above the enthesis, the cross-sectional area of primary tendon fibers was 38% that of the whole tendon (0.23 ± 0.04 mm^2), significantly smaller than the primary insertion area (Fig. S1 B, C).

Notes on mechanical testing, enthesis strength, and enthesis toughness

Loading specimens secured with the custom 3D printed fixtures and novel slidable gripping system (Fig. S17) produced force-displacement responses that were highly repeatable (Fig. S3B) and, if needed, interruptible and fixable at prescribed loading/displacement levels. These fixtures also allowed specimens to be recovered post-testing at their failure displacements.

Identifying local strain via conventional optical strain tracking was not possible with the current experimental setup. The bulk tendon is covered by a non load-bearing sheath that does not deform along with the underlying tendon enthesis (Fig. S1A, blue dotted line). In all failed samples, the sheath was intact post failure (Fig. S3A, transparent tissue). Staining the enthesis samples with Verhoeff's stain to create a speckle pattern in tracking the strain was therefore only able to track sheath surface strain.

In the current paper, we use the nomenclature "strength" (experimentally obtained as a failure load when samples fail) and "toughness" (experimentally obtained as a work to failure, the area under force-displacement curve) to describe the structural properties of mouse entheses. We do not normalize the measurements because: (1) the underlying geometry and local strain of the tendon enthesis could not be defined and (2) tendon entheses did not fail where peak stresses might intuitively be expected (i.e., at the tendon minimum cross-sectional area).

Notes on avulsed (fractured) pieces

To investigate the energy absorption with enthesis failure, we characterized avulsed bony pieces using high resolution microCT. Avulsion area and/or the number of avulsed fragments changed with the loading regime, loading position, and *in vivo* loading conditions. For example, the results for monotonic increases in loading rate showed that the healthy enthesis loaded at high loading rate stored and dissipate enough energy to either propagate its crack to a larger than primary insertion area bony avulsed piece, or from many bony fragments. This failure pattern is consistent with previous observations on rate-sensitivity of bone fracture (*64*, *65*).

Positional-recruitment Model

The model idealizes the geometry of humeral head (circular bone ridge) and N linear elastic fibers with thickness t, each spaced a distance s apart make up tendon to bone attachment, beginning with a fiber that is immediately to the left of a circular bone ridge of radius R (Fig.S18).

The centerline of fiber n inserts into the bone at position:

$$\vec{r}_0^{\,n} = -x_0^n\hat{\imath} + 0\hat{\jmath} \tag{S1}$$

where $\hat{\imath}$ and $\hat{\jmath}$ are unit vectors parallel to the x and y axes, respectively, shown in Fig. S5 and Fig. S18, and

$$x_0^n = R + \frac{t}{2} + (n-1)s \tag{S2}$$

is position of the fiber insertion (red circles at the insertion in the Fig. S5, taut). To note, s>t as s is midline of fiber to midline of next fiber.

We assume that the initial (at rest) length of outer fiber should be larger than inner fiber. The innermost fiber (a fiber that is immediately to the left of a circular bone ridge) is the shortest, and fiber length increases with the distance *s*. This allowed us to represent that: (1) the outer (bursal side) fibers longer than the inner (articular side) fibers, making the innermost fiber (n=1) shortest and (2) tendon fibers are buckled at high angles of abduction. Before defining the initial fiber length L_0^n, we derive the posture-dependent fiber engagement theory. If the fiber is engaged and is oriented so that it contacts the bone ridge, then it tightens until it reaches the tangent point (blue circles) to the humeral head curvature (Fig. 2A, Fig. S5, and Fig.S13):

$$\vec{r}_1^n = R^n(-\cos\phi_1^n\,\hat{\imath} + \sin\phi_1^n\,\hat{\jmath}) \quad \text{(S3)}$$

The radius of the centerline of the wrapped fiber (when the curvature of bony ridge takes an effect) is:

$$R^n = R + \left(n - \frac{1}{2}\right)t \quad \text{(S4)}$$

The contact angle (the angle at which engaged fibers contact the bone ridge and can no longer tighten), is found at

$$\cos\phi_1^n = R^n/x_0^n. \quad \text{(S5)}$$

The grip holds all fibers in the order they are attached to the bone. When the grip is turned an angle θ (black arrow) to represent postural change then stretched in a direction $\hat{e}$, the angle at which contact is lost is determined by the innermost fiber, assumed to always stay in tension. Contact is lost at the point $\vec{r}_2^n(t)$ at which the unit vector between $\vec{r}_2^n(t)$ and the connection point on the grip for the strand, $\vec{r}_3^n(t)$, is tangent to the circle formed by the midline of fiber n:

$$(\vec{r}_3^{\,n}(t) - \vec{r}_2^{\,n}(t)) \cdot \vec{r}_2^{\,n}(t) = 0, \tag{S6}$$

or

$$\vec{r}_3^{\,n}(t) \cdot (-\cos\phi_2^n\,(t)\hat{\imath} + \sin\phi_2^n(t)\,\hat{\jmath}) = R^n. \tag{S7}$$

Writing $\vec{r}_3^{\,n}(t) = r_3^n(e_{3x}^n(t)\hat{\imath} + e_{3y}^n(t)\hat{\jmath})$, ϕ_2^n can be solved from:

$$\cos\phi_2^n\,(t) = \left(\frac{R^n}{r_3^n}\right)\left(-e_{3x}^n + \sqrt{(e_{3x}^n)^2 + \left(e_{3y}^n\right)^2\left(\frac{r_3^n}{R^n}\right)^2 - 1}\right). \tag{S8}$$

The grip is placed so that the innermost fiber is not in tension when the tendon is pulled horizontally. Tension starts with $\theta = 0$ and fibers aligned with the $\hat{\imath}$ direction, and with fiber n connected at:

$$\vec{r}_3^{\,n}(0^-) = x_3^0\hat{\imath} + R^n\hat{\jmath}, \tag{S9}$$

where x_3^0 is the same for all fibers. The grip is then rotated by an angle θ about the center of the insertion site, so that:

$$\vec{r}_3^{\,n}(0^+) = \mathbf{Q}(\theta)(\vec{r}_3^{\,n}(0^-) - \langle\vec{r}_0^{\,n}\rangle), \tag{S10}$$

where, for evenly spaced fibers, the insertion is centered at the average position $\langle\vec{r}_0^{\,n}\rangle = \frac{1}{2}(\vec{r}_0^{\,N} + \vec{r}_0^{\,1})$, and the rotation matrix is:

$$\mathbf{Q}(\theta) = \begin{bmatrix}\cos\theta & -\sin\theta\\ \sin\theta & \cos\theta\end{bmatrix}. \tag{S11}$$

Now, as we previously assumed, the initial (at rest) length of outer fiber should be larger than the inner fiber. The inner most fiber (a fiber that is immediately to the left of a circular bone ridge) is the shortest, and fiber length increases with the distance s, then initial length for n$^{\text{th}}$ fiber can be expressed as:

$$L_0^n(t) = (\phi_2^n)R_0^n + \|\vec{r}_3^n(t) - \vec{r}_2^n(t)\|, \tag{S12}$$

where $R_0^n = \|\vec{r}_0^n\| = R + \frac{t}{2} + (n-1)s$.

The maximum length of a fiber for it to be engaged when contacting other fibers on the bone ridge is then:

$$L_{en}^n(t) = \|\vec{r}_1^n - \vec{r}_0^n\| + (\phi_2^n(t) - \phi_1^n)R^n + \|\vec{r}_3^n(t) - \vec{r}_2^n(t)\|, \tag{S13}$$

where ϕ_1^n and $\phi_2^n(t)$ are in radians.

Another possibility is that the fiber is engaged but does not contact the fibers around the bone ridge. This occurs when where $\phi_2^n(t) < \phi_1^n$ and:

$$\frac{\vec{r}_3^n(t) - \vec{r}_0^n}{\|\vec{r}_3^n(t) - \vec{r}_0^n\|} \cdot \hat{\jmath} \equiv \hat{e}_{03}(t) \cdot \hat{\jmath} < \frac{\vec{r}_1^n(t) - \vec{r}_0^n}{\|\vec{r}_1^n(t) - \vec{r}_0^n\|} \cdot \hat{\jmath} \equiv \hat{e}_{10}(t) \cdot \hat{\jmath}. \tag{S14}$$

In this case,

$$L_{en}^n(t) = \|\vec{r}_3^n(t) - \vec{r}_0^n\|. \tag{S15}$$

We generated load-displacement curves from this posture depending fiber kinematic model. To simplify fibers were assumed to be elastic, brittle, and frictionless.

The stretch ratio was calculated as follows:

$$\lambda^n(t) = \begin{cases} 1, & L_{en}^n(t) \leq L^n(0) \\ \dfrac{L_{en}^n(t)}{L^n(0)}, & L_{en}^n(t) > L^n(0) \end{cases}. \tag{S16}$$

A linear constitutive law was used for analysis:

$$F^n(t) = \begin{cases} 0, & \lambda^n(t) \leq 1 \\ K(\lambda^n(t) - 1), & \lambda^n(t) > 1 \end{cases} \tag{S17}$$

where *K* was the modulus (stiffness) of the enthesis fibers.

The model parameters used for positional recruitment model simulations were determined from high resolution contrast enhanced microCT images of mice supraspinatus tendon enthesis (n=4 biological replicates). Failure strain were determined based on the experimental set-up and the data obtained from the healthy tendon enthesis (Fig. S3B). Model gauge lengths, $Min\ L^n(0)$, were set to 2.5 mm, the lengths used in *ex vivo* experiments. To ease the normalization processes, the tendon enthesis fiber bulk stiffness was set to 1. The supraspinatus tendon enthesis measurements and model parameters used for positional recruitment simulation is represented in Table S1.

To assess the role of failure strain and fiber spacing on positional recruitment model simulations, a sensitivity analysis was performed. Although the magnitude of the failure stress varied with the choice of failure strain, the trade-offs between strength and toughness did not (Fig. S19). Normalized strength and stiffness were relatively sensitive, while toughness was mostly relatively insensitive to the choice of fiber spacing for lower abduction angles (<90°), but more sensitive for higher abduction angles (Fig. S20). Toughness decreased monotonically with fiber spacing (Fig. S20).

Enthesis fracture model

To estimate the contribution of local bony architecture on the tendon enthesis failure behavior, we adapted a previously published plate-in-bending model *(16)* where loading at the tendon enthesis is modeled as a circular clamped plate loaded with uniform pressure (Fig. S14). In this model, the circular plate represents the tendon enthesis and its mineralized base (i.e., the mineralized fibrocartilage and the cortical shell) and is clamped at the edges by load-bearing trabeculae (i.e., trabecular plates).

The mineralized bone plug is assumed to be thin relative to its radius, hence shear deformability is ignored. The displacement field in this plate-in-bending model can be expressed as (63):

$$w(r) = w_{max}\left(\left(\frac{r}{a}\right)^2 - 1\right)^2, \tag{S18}$$

where $w_{max} = pa^4/(64D)$, a is the distance between the clamps (i.e., trabecular spacing), p is the applied pressure (i.e., force), and D is the plate bending modulus that is proportional to elastic modulus, E, and cube of the plate thickness t (i.e., cortical thickness). The potential energy, U, in the bone at the plate is:

$$PE(a) = -\pi \int_0^a w(r) r dr = -\frac{\pi a^6 p^2}{384D}. \tag{S19}$$

The upper bound on toughness comes from assuming that the tendon holds negligible stored energy just prior to bone avulsion, as in the fiber recruitment model. With the assumption that the process zone is small compared with other dimensions, the energy balance for bone avulsion is:

$$U(a) = \pi a^2 \Gamma_{int}, \tag{S20}$$

where Γ_{int} is the critical energy release rate of the interface that fractures or, in the case of a penny-shaped crack in the cortical bone, the critical energy release rate of the cortical bone.

For removal of a bone plug, the energy balance becomes:

$$U(a) = \pi a t \mathit{\Gamma}_0, \tag{S21}$$

where $\mathit{\Gamma}_0$ is the energy per unit area for removal of a bone plug.

Healthy tendon entheses fail at the mineralized fibrocartilage and cortical shell interface (MF-B failure type) and at the trabecular interface (B-T failure type) at relatively similar rates. By assuming that all the potential energy is converted to failing the tendon enthesis, the fracture toughness of the tendon enthesis, Γ_{int}, will be expressed as

$$\Gamma_{int} = \frac{a^4 p^2}{384D}. \tag{S22}$$

To investigate the contribution of trabecular spacing and the mineralized base on enthesis strength and fracture toughness, we used the above equation to conduct numerical simulations by varying each parameter by ±50%. Results of this simulations are shown in Fig. S15.

Table S1.

Model parameters used for postural recruitment analysis.

	Parameter	Measurements (n=6 biological replicates, mean ± SD)	Model Value
Number of fibers	N	20.17 ± 2.17	20
Fiber thickness (mm)	t	9.98E-3 ± 2.58E-3	0.01
Distance between fibers (mm)	s	0.0154 ± 0.00431	0.015
Humeral head radius (mm)	R	1.022 ± 0.069	1
Failure strain	$max\frac{L_{en}^{n}(t)}{L^{n}(0)}$	0.220 ± 0.041	0.2

Descriptions of Movies S1 to S4

Movie S1.
3D volume rendering of intact mouse enthesis samples. Artificial coloring was added to help visualize the tendon enthesis.

Movie S2.
2D image stacks of a representative failed tendon enthesis sample.

Movie S3.
3D visualization of a representative failure crater where the tendon enthesis is failed. The images were obtained using high-resolution convectional microCT at sub-micrometer resolution (0.75 μm).

Movie S4.
3D visualization of mouse glenohumeral joint visualized using contrast enhanced microCT technique.

REFERENCES AND NOTES

1. Z. Yin, F. Hannard, F. Barthelat, Impact-resistant nacre-like transparent materials. *Science* **364**, 1260–1263 (2019).

2. Y. Liu, N. A. Fleck, V. S. Deshpande, A. Srivastava, High fracture toughness micro-architectured materials. *J. Mech. Phys. Solids* **143**, 104060 (2020).

3. N. A. Fleck, V. S. Deshpande, M. F. Ashby, Micro-architectured materials: Past, present and future. *Proc. R. Soc. A Math. Phys. Eng. Sci.* **466**, 2495–2516 (2010).

4. M. Mirkhalaf, A. K. Dastjerdi, F. Barthelat, Overcoming the brittleness of glass through bio-inspiration and micro-architecture. *Nat. Commun.* **5**, 3166 (2014).

5. F. Barthelat, Z. Yin, M. J. Buehler, Structure and mechanics of interfaces in biological materials. *Nat. Rev. Mater.* **1**, 16007 (2016).

6. F. Barthelat, Architectured materials in engineering and biology: Fabrication, structure, mechanics and performance. *Int. Mater. Rev.* **60**, 412–430 (2015).

7. R. O. Ritchie, The conflicts between strength and toughness. *Nat. Mater.* **10**, 817–822 (2011).

8. G. M. Genin, S. Thomopoulos, The tendon-to-bone attachment: Unification through disarray. *Nat. Mater.* **16**, 607–608 (2017).

9. L. Rossetti, L. A. Kuntz, E. Kunold, J. Schock, K. W. Müller, H. Grabmayr, J. Stolberg-Stolberg, F. Pfeiffer, S. A. Sieber, R. Burgkart, A. R. Bausch, The microstructure and micromechanics of the tendon-bone insertion. *Nat. Mater.* **16**, 607–608 (2017).

10. S. Thomopoulos, G. R. Williams, J. A. Gimbel, M. Favata, L. J. Soslowsky, Variation of biomechanical, structural, and compositional properties along the tendon to bone insertion site. *J. Orthop. Res.* **21**, 413–419 (2003).

11. A. C. Deymier-Black, J. D. Pasteris, G. M. Genin, S. Thomopoulos, Allometry of the tendon enthesis: Mechanisms of load transfer between tendon and bone. *J. Biomech. Eng.* **137**, 111005 (2015).

12. S. P. Lake, K. S. Miller, D. M. Elliott, L. J. Soslowsky, Effect of fiber distribution and realignment on the nonlinear and inhomogeneous mechanical properties of human supraspinatus tendon under longitudinal tensile loading. *J. Orthop. Res.* **27**, 1596–1602 (2009).

13. S. Thomopoulos, J. P. Marquez, B. Weinberger, V. Birman, G. M. Genin, Collagen fiber orientation at the tendon to bone insertion and its influence on stress concentrations. *J. Biomech.* **39**, 1842–1851 (2006).

14. G. M. Genin, A. Kent, V. Birman, B. Wopenka, J. D. Pasteris, P. J. Marquez, S. Thomopoulos, Functional grading of mineral and collagen in the attachment of tendon to bone. *Biophys. J.* **97**, 976–985 (2009).

15. Y. Hu, V. Birman, A. Demyier-Black, A. G. Schwartz, S. Thomopoulos, G. M. Genin, Stochastic interdigitation as a toughening mechanism at the interface between tendon and bone. *Biophys. J.* **108**, 431–437 (2015).

16. A. C. Deymier, A. G. Schwartz, Z. Cai, T. L. Daulton, J. D. Pasteris, G. M. Genin, S. Thomopoulos, The multiscale structural and mechanical effects of mouse supraspinatus muscle unloading on the mature enthesis. *Acta Biomater.* **83**, 302–313 (2019).

17. M. J. Buehler, Molecular nanomechanics of nascent bone: Fibrillar toughening by mineralization. *Nanotechnology* **18**, 295102 (2007).

18. M. S. Rashid, C. Cooper, J. Cook, D. Cooper, S. G. Dakin, S. Snelling, A. J. Carr, Increasing age and tear size reduce rotator cuff repair healing rate at 1 year. *Acta Orthop.* **88**, 606–611 (2017).

19. L. M. Galatz, C. M. Ball, S. A. Teefey, W. D. Middleton, K. Yamaguchi, The outcome and repair integrity of completely arthroscopically repaired large and massive rotator cuff tears. *J. Bone Jt. Surg. Ser. A* **86**, 219–224 (2004).

20. J. Sartori, H. Stark, Tracking tendon fibers to their insertion—A 3D analysis of the Achilles tendon enthesis in mice. *Acta Biomater.* **120**, 146–155 (2021).

21. Y. Liu, V. Birman, C. Chen, S. Thomopoulos, G. M. Genin, Mechanisms of bimaterial attachment at the interface of tendon to bone. *J. Eng. Mater. Technol.* **133**, 011006 (2010).

22. F. Saadat, A. C. Deymier, V. Birman, S. Thomopoulos, G. M. Genin, The concentration of stress at the rotator cuff tendon-to-bone attachment site is conserved across species. *J. Mech. Behav. Biomed. Mater.* **62**, 24–32 (2016).

23. H. M. Shaw, M. Benjamin, Structure-function relationships of entheses in relation to mechanical load and exercise. *Scand. J. Med. Sci. Sports* **17**, 303–315 (2007).

24. J. M. Weiss, A. Arkader, L. M. Wells, T. J. Ganley, Rotator cuff injuries in adolescent athletes. *J. Pediatr. Orthop. Part B.* **22**, 133–137 (2013).

25. J. Y. Jeong, S. K. Min, K. M. Park, Y. B. Park, K. J. Han, J. C. Yoo, Location of rotator cuff tear initiation: A magnetic resonance imaging study of 191 shoulders. *Am. J. Sports Med.* **46**, 649–655 (2018).

26. H. M. Kim, N. Dahiya, S. A. Teefey, W. D. Middleton, G. Stobbs, K. Steger-May, K. Yamaguchi, J. D. Keener, Location and initiation of degenerative rotator cuff tears: An analysis of three hundred and sixty shoulders. *J. Bone Jt. Surg. Ser. A* **92**, 1088–1096 (2010).

27. K. Yamaguchi, K. Ditsios, W. D. Middleton, C. F. Hildebolt, L. M. Galatz, S. A. Teefey, The demographic and morphological features of rotator cuff disease: A comparison of asymptomatic and symptomatic shoulders. *J. Bone Jt. Surg. Ser. A* **88**, 1699–1704 (2006).

28. M. I. Danto, S. L. Woo, The mechanical properties of skeletally mature rabbit anterior cruciate ligament and patellar tendon over a range of strain rates. *J. Orthop. Res.* **11**, 58–67 (1993).

29. H. A. Lynch, W. Johannessen, J. P. Wu, A. Jawa, D. M. Elliott, Effect of fiber orientation and strain rate on the nonlinear uniaxial tensile material properties of tendon. *J. Biomech. Eng.* **125**, 726–731 (2003).

30. J. L. Zitnay, G. S. Jung, A. H. Lin, Z. Qin, Y. Li, S. M. Yu, M. J. Buehler, J. A. Weiss, Accumulation of collagen molecular unfolding is the mechanism of cyclic fatigue damage and failure in collagenous tissues. *Sci. Adv.* **6**, eaba2795 (2020).

31. J. L. Zitnay, Y. Li, Z. Qin, B. H. San, B. Depalle, S. P. Reese, M. J. Buehler, S. M. Yu, J. A. Weiss, Molecular level detection and localization of mechanical damage in collagen enabled by collagen hybridizing peptides. *Nat. Commun.* **8**, 14913 (2017).

32. S. P. McCully, N. Kumar, M. D. Lazarus, A. R. Karduna, Internal and external rotation of the shoulder: Effects of plane, end-range determination, and scapular motion. *J. Shoulder Elb. Surg.* **14**, 605–610 (2005).

33. M. D. Newton, A. A. Davidson, R. Pomajzl, J. Seta, M. D. Kurdziel, T. Maerz, The influence of testing angle on the biomechanical properties of the rat supraspinatus tendon. *J. Biomech.* **49**, 4159–4163 (2016).

34. K. Lindblom, On pathogenesis of ruptures of the tendon aponeurosis of the shoulder joint. *Acta Radiol.* **20**, 564–577 (1939).

35. C. Y. Huang, V. M. Wang, R. J. Pawluk, J. S. Bucchieri, W. N. Levine, L. U. Bigliani, V. C. Mow, E. L. Flatow, Inhomogeneous mechanical behavior of the human supraspinatus tendon under uniaxial loading. *J. Orthop. Res.* **23**, 924–930 (2005).

36. H. Ouellette, J. Labis, M. Bredella, W. E. Palmer, K. Sheah, M. Torriani, Spectrum of shoulder injuries in the baseball pitcher. *Skelet. Radiol.* **37**, 491–498 (2008).

37. O. A. Tertuliano, J. R. Greer, The nanocomposite nature of bone drives its strength and damage resistance. *Nat. Mater.* **15**, 1195–1202 (2016).

38. C. Gerber, J. G. Snedeker, D. Baumgartner, A. F. Viehöfer, Supraspinatus tendon load during abduction is dependent on the size of the critical shoulder angle: A biomechanical analysis. *J. Orthop. Res.* **32**, 952–957 (2014).

39. Z. L. Shen, H. Kahn, R. Ballarini, S. J. Eppell, Viscoelastic properties of isolated collagen fibrils. *Biophys. J.* **100**, 3008–3015 (2011).

40. J. Liu, D. Das, F. Yang, A. G. Schwartz, G. M. Genin, S. Thomopoulos, I. Chasiotis, Energy dissipation in mammalian collagen fibrils: Cyclic strain-induced damping, toughening, and strengthening. *Acta Biomater.* **80**, 217–227 (2018).

41. Y. Liu, S. Thomopoulos, C. Chen, V. Birman, M. J. Buehler, G. M. Genin, Modelling the mechanics of partially mineralized collagen fibrils, fibres and tissue. *J. R. Soc. Interface* **11**, 20130835 (2014).

42. A. C. Deymier, Y. An, J. J. Boyle, A. G. Schwartz, V. Birman, G. M. Genin, S. Thomopoulos, A. H. Barber, Micro-mechanical properties of the tendon-to-bone attachment. *Acta Biomater.* **56**, 25–35 (2017).

43. I. M. Basalo, F. H. Chen, C. T. Hung, G. A. Ateshian, Frictional response of bovine articular cartilage under creep loading following proteoglycan digestion with chondroitinase ABC. *J. Biomech. Eng.* **128**, 131–134 (2006).

44. O. G. Andriotis, S. Desissaire, P. J. Thurner, Collagen fibrils: Nature's highly tunable nonlinear springs. *ACS Nano* **12**, 3671–3680 (2018).

45. D. R. Carter, Mechanical loading histories and cortical bone remodeling. *Calcif. Tissue Int.* **36**, S19-S24 (1984).

46. L. B. Meakin, J. S. Price, L. E. Lanyon, The contribution of experimental in vivo models to understanding the mechanisms of adaptation to mechanical loading in bone. *Front. Endocrinol.* **5**, 154 (2014).

47. A. M. Tatara, J. H. Lipner, R. Das, H. M. Kim, N. Patel, E. Ntouvali, M. J. Silva, S. Thomopoulos, The role of muscle loading on bone (re)modeling at the developing enthesis. *PLOS ONE* **9**, e97375 (2014).

48. X. S. Liu, P. Sajda, P. K. Saha, F. W. Wehrli, G. Bevill, T. M. Keaveny, X. E. Guo, Complete volumetric decomposition of individual trabecular plates and rods and its morphological correlations with anisotropic elastic moduli in human trabecular bone. *J. Bone Miner. Res.* **23**, 223–235 (2008).

49. E. R. Cadet, J. W. Hsu, W. N. Levine, L. U. Bigliani, C. S. Ahmad, The relationship between greater tuberosity osteopenia and the chronicity of rotator cuff tears. *J. Shoulder Elb. Surg.* **17**, 73–77 (2008).

50. F. Barthelat, H. D. Espinosa, An experimental investigation of deformation and fracture of nacre-mother of pearl. *Exp. Mech.* **47**, 311–324 (2007).

51. V. Imbeni, J. J. Kruzic, G. W. Marshall, S. J. Marshall, R. O. Ritchie, The dentin-enamel junction and the fracture of human teeth. *Nat. Mater.* **4**, 229–232 (2005).

52. F. Marin, N. Le Roy, B. Marie, The formation and mineralization of mollusk shell. *Front. Biosci.* **4**, 1099–1125 (2012).

53. K. Livanov, H. Jelitto, B. Bar-On, K. Schulte, G. A. Schneider, D. H. Wagner, Tough alumina/polymer layered composites with high ceramic content. *J. Am. Ceram. Soc.* **98**, 1285–1291 (2015).

54. B. Han, K. K. Qin, B. Yu, Q. C. Zhang, C. Q. Chen, T. J. Lu, Design optimization of foam-reinforced corrugated sandwich beams. *Compos. Struct.* **130**, 51–62 (2015).

55. S. Khandelwal, T. Siegmund, R. J. Cipra, J. S. Bolton, Transverse loading of cellular topologically interlocked materials. *Int. J. Solids Struct.* **49**, 2394–2403 (2012).

56. M. Carlesso, R. Giacomelli, T. Krause, A. Molotnikov, D. Koch, S. Kroll, K. Tushtev, Y. Estrin, K. Rezwan, Improvement of sound absorption and flexural compliance of porous alumina-mullite ceramics by engineering the microstructure and segmentation into topologically interlocked blocks. *J. Eur. Ceram. Soc.* **33**, 2549–2558 (2013).

57. M. B. Schmidt, V. C. Mow, L. E. Chun, D. R. Eyre, Effects of proteoglycan extraction on the tensile behavior of articular cartilage. *J. Orthop. Res.* **8**, 353–363 (1990).

58. S. Cavelier, A. K. Dastjerdi, M. D. McKee, F. Barthelat, Bone toughness at the molecular scale: A model for fracture toughness using crosslinked osteopontin on synthetic and biogenic mineral substrates. *Bone* **110**, 304–311 (2018).

59. I. Kurtaliaj, M. Golman, A. C. Abraham, S. Thomopoulos, Biomechanical testing of murine tendons. *J. Vis. Exp.*, (2019).

60. S. W. Linderman, M. Golman, T. R. Gardner, V. Birman, W. N. Levine, G. M. Genin, S. Thomopoulos, Enhanced tendon-to-bone repair through adhesive films. *Acta Biomater.* **70**, 165–176 (2018).

61. F. Fang, S. P. Lake, Multiscale mechanical integrity of human supraspinatus tendon in shear after elastin depletion. *J. Mech. Behav. Biomed. Mater.* **63**, 443–455 (2016).

62. A. C. Abraham, S. A. Shah, M. Golman, L. Song, X. Li, I. Kurtaliaj, M. Akbar, N. L. Millar, Y. Abu-Amer, L. M. Galatz, S. Thomopoulos, Targeting the NF-kB signaling pathway in chronic tendon disease. *Sci. Transl. Med.* **11**, eaav4319 (2019).

63. V. Birman, *Plate Structures* (Springer Science and Business media, 2011).

64. M. M. Panjabi, A. A. White, W. O. Southwick, Mechanical properties of bone as a function of rate of deformation. *J. Bone Joint Surg. Am.* **55**, 322–330 (1973).

65. T. M. Wright, W. C. Hayes, Tensile testing of bone over a wide range of strain rates: Effects of strain rate, microstructure and density. *Med. Biol. Eng.* **14**, 671–680 (1976).